*fluids*

MDPI

*Article*

# Residence-Time-Dependent Evolution of the Protein Matrix Modulates Nucleation and Pattern Formation in Drying Protein Droplets

**Hector Alexander Macias-Albores [1], Iris G. Velasco-Terán [1], Orlando Díaz-Hernandez [1], Heber Vilchis-Bravo [2], Yojana J. P. Carreón [1,3,4,*] and Jorge González-Gutiérrez [1,*]**

[1] Facultad de Ciencias en Física y Matemáticas, Universidad Autónoma de Chiapas, Calzada Emiliano Zapata Km. 8, Loma Bonita, Terán, Tuxtla Gutiérrez 29055, Chiapas, Mexico; x180068@unach.mx (H.A.M.-A.); x180069@unach.mx (I.G.V.-T.); orlando.diaz@unach.mx (O.D.-H.)
[2] Institute for Research and Innovation in Renewable Energies, University of Science and Arts of Chiapas, Libramiento Nte. Pte. 1150. Lajas Maciel, Tuxtla Gutiérrez 25900, Chiapas, Mexico; heber.vilchis@unicach.mx
[3] Facultad de Medicina Veterinaria y Zootecnia, Universidad Autónoma de Chiapas, Calzada Emiliano Zapata Km. 8, Loma Bonita, Terán, Tuxtla Gutiérrez 29055, Chiapas, Mexico
[4] Ministry of Science, Humanities, Technology and Innovation, México City 03940, Mexico
* Correspondence: yojana.carreon@unach.mx (Y.J.P.C.); jorge.ggutierrez@unach.mx (J.G.-G.)

## Abstract

The formation of internal patterns in drying protein droplets is commonly interpreted as a consequence of evaporation-driven hydrodynamic transport. Here, we show that the residence time of the HSA–NaCl system before the hygrometric transition systematically modulates the morphology of the final dried deposit. By varying the residence time before the hygrometric transition ($t_r$), that is, the time for which the droplet is kept at high relative humidity, we controlled the duration of the pre-transition evolution of the protein matrix before accelerated drying. Short residence times produced heterogeneous aggregates, whereas prolonged residence favored coherent dendritic deposits with higher inter-sample reproducibility. These results are consistent with the interpretation that time-dependent structural evolution of the gel matrix constrains the accessible nucleation pathways and thereby influences the final deposit geometry. Multiscale morphological analysis based on texture descriptors, directional coherence, and radial features, combined with principal component analysis (PCA) and Gaussian mixture modeling, revealed residence-time-dependent changes in morphological organization, together with a progressive reduction in the number of recurrent morphotypes at prolonged residence times. Atomic force microscopy showed a parallel change in surface relief, from dispersed micro-islands and isolated peaks at short residence times to recurrent topographic motifs after prolonged residence. Nucleation dynamics changed from spatially distributed competitive growth at short residence times to highly localized and recurrent nucleation from a reduced number of reproducible sites at long residence times. Time-resolved lateral profiles showed similar early thinning trajectories under high relative humidity, while also revealing that solvent loss occurs during the residence stage: the hygrometric transition was applied to a still-curved droplet at short residence time and to a macroscopically flattened matrix at prolonged residence times. Together, these results indicate that the residence time, $t_r$, before the hygrometric transition modulates the nucleation regime and final architecture of protein deposits.

**Keywords:** drying droplets; protein gelation; hygrometric transition; protein matrix evolution; nucleation pathways; dendritic pattern formation; atomic force microscopy

Check for updates

Academic Editor: Rajinder Pal

Received: 21 August 2026
Revised: 23 September 2026
Accepted: 24 September 2026
Published: 26 September 2026

**Copyright:** © 2026 by the authors. Licensee MDPI, Basel, Switzerland. This article is an open access article distributed under the terms and conditions of the Creative Commons Attribution (CC BY) license.

## 1. Introduction

Drying droplets on solid substrates can transform solvent loss, internal transport, and solute accumulation into complex solid patterns that act as physicochemical fingerprints of the molecular state of a solution. The final deposit preserves, in a spatially resolved form, the effects of evaporation, contact-line pinning, concentration gradients, interfacial flow, and out-of-equilibrium solidification [1–3]. In colloidal systems, the resulting organization is also strongly influenced by particle interactions and geometrical constraints, which can regulate ordering, defect formation, and the selection of accessible assembled configurations [4]. Under drying conditions, these coupled processes generate peripheral rings, radial deposits, branched structures, and dendritic morphologies, whose spatial distribution reflects the balance between capillary transport, local accumulation, and solidification [5–8]. In droplets containing biological macromolecules, solvent removal proceeds together with conformational rearrangement, aggregation, and physical network formation [9–11]. Dried protein droplets therefore preserve both evaporative transport signatures and the structural history acquired by the macromolecular phase during concentration, gelation, and arrest.

The classical description of pattern formation in drying droplets is based primarily on evaporation-induced transport. The vapor pressure difference between the liquid–vapor interface and the surrounding atmosphere drives solvent diffusion into the gas phase and determines the macroscopic mass-loss rate [12–15]. Nonuniform evaporation along the droplet surface generates internal flows that replenish liquid near regions of higher solvent loss [16–18]. Under contact-line pinning, these flows promote solute accumulation near the edge and favor coffee-ring formation [19,20]. Marangoni stresses, thermal gradients, compositional gradients, and interfacial adsorption can further redistribute the solute and produce more complex architectures [21–23]. Such emergent phenomena are most effective when the suspended or dissolved material remains mobile during most of the evaporation process.

In protein-containing gelling systems, the solute phase progressively loses mobility as a percolated macromolecular network develops inside the droplet. The system evolves from a transport-dominated liquid toward a mechanically constrained medium whose internal organization depends on network connectivity, local concentration, and structural relaxation. The sol–gel transition reduces the configurational freedom of the macromolecules, increases the effective relaxation time, and restricts the pathways available for diffusion, aggregation, and local rearrangement [24–29]. Solvent removal remains governed by the vapor pressure gradient. As gelation progresses, the evolving state of the protein-rich matrix may increasingly influence the organization of the material remaining on the substrate. The final pattern can therefore reflect the coupling between evaporation-driven concentration and the structural evolution of the macromolecular phase before complete drying.

Protein droplets are particularly sensitive to this coupling because proteins form transient physical networks through hydrogen bonding, hydrophobic association, electrostatic interactions, ionic bridging, and salt-mediated coordination [25,27]. During drying, these interactions evolve within a confined droplet where concentration gradients, contact-line pinning, local dehydration, and internal flows occur simultaneously [18,20,30]. As protein concentration increases, the effective volume fraction rises, free volume decreases, and the matrix can enter a physically aged regime associated with reduced cooperative mobility and longer configurational relaxation times [29,31,32]. Therefore, the post-gel aging interval, $t_g$, provides additional time for structural evolution of the concentrated protein matrix before the final drying stage.

As the network consolidates, the routes available for solid architecture formation may become progressively restricted. In an early or weakly organized gel, residual mobility can

support multiple aggregation routes, spatially distributed nucleation events, and competition among several growth fronts [33]. In a more structurally organized gel, molecular rearrangement may become increasingly constrained, reducing the number of growth pathways available to the system [33,34]. Conceptually, the competition between structural relaxation and solvent removal can be represented by the ratio $\tau_{relax}/\tau_{dry}$. This ratio is used here only as a qualitative framework, since neither timescale was measured directly.

The morphology of the final deposit can therefore be interpreted as a spatial record of the organization reached by the gelled protein matrix before complete drying. Within an energy-landscape framework, a weakly organized network may be associated with a broader set of accessible configurations, favoring dispersed nucleation and higher pattern variability [35,36]. Progressive structural consolidation may, in turn, restrict the set of rearrangement and aggregation pathways available to the system [29,31,37]. These energy-landscape concepts are used here as a qualitative interpretive framework and are not directly measured in the present experiments. In this regime, the final pattern can be interpreted as resulting from coupled transport, time-dependent matrix evolution, and kinetic arrest.

Nanoscale surface topography complements the morphological analysis by resolving the surface relief formed during the late-stage immobilization and densification of the protein-rich matrix [38,39]. Nanometric features provide morphological traces of the organization reached by the network prior to complete drying and help evaluate how the internal state of the gel contributes to pattern selection. Integrated with multiscale morphology and nucleation analysis, topographic characterization links the final surface architecture with the pre-drying organization of the protein network. The surface relief therefore records late-stage immobilization events occurring as the hydrated gelled matrix becomes a dry deposit.

The residence-time protocol used here shares a general conceptual similarity with other processing strategies in which the prehistory of a material influences a subsequent structural transition, but the underlying physical processes are distinct. In materials annealing, structural reorganization is typically promoted by a controlled thermal treatment that enhances molecular or atomic mobility and can drive the system toward more stable configurations. In the residence-time protocol considered here, no thermal annealing step is applied; instead, the matrix evolves isothermally under high relative humidity before an abrupt hygrometric transition increases the evaporative driving force. A related distinction applies to controlled nucleation in lyophilization, where nucleation is deliberately induced during freezing to regulate ice-crystal formation and the subsequent sublimation stage. Here, no freezing or sublimation occurs, and the observed nucleation and dendritic growth are triggered during evaporative concentration following a humidity decrease. The common element among these processes is therefore the sensitivity of later-stage morphology to the physicochemical history established before the final transformation, whereas the control variable and phase-transition mechanism are different.

From an application perspective, controlling the morphology and reproducibility of dried protein deposits is relevant to processes in which protein-containing droplets are deposited onto solid substrates, including biofunctional coatings, controlled deposition, and evaporation-based printing. In these systems, spatially heterogeneous accumulation, uncontrolled branching, and sample-to-sample variability can affect surface coverage and the resulting deposit architecture. Humidity history and the time elapsed before final drying therefore represent potentially useful processing variables for modulating nucleation localization and morphological reproducibility in protein-containing formulations.

Extensive work has addressed drying droplets, coffee-ring formation, protein aggregation, and physical gelation. However, the role of the residence time before the hygrometric

transition, $t_r$, and the associated post-gel aging interval, $t_g$, in pattern selection remains insufficiently established. In particular, it is unclear how the pre-transition evolution of a gel-forming protein matrix affects the number and localization of nucleation events and the reproducibility of the final deposit. Addressing this question requires an experimental framework in which the residence time is varied before applying a reproducible hygrometric trigger.

In this work, we examine how the residence time of the HSA–NaCl matrix prior to the humidity transition influences the morphology of deposits formed by drying droplets. The residence time before the hygrometric transition, $t_r$, was systematically varied from a pre-gel condition to progressively longer post-gel residence intervals before triggering the final drying process. For post-gel conditions, this variation corresponded to increasing post-gel aging times, $t_g$. The resulting deposits were analyzed by integrating multiscale morphology, nucleation kinetics, dimensionality-reduction analysis, probabilistic modeling, and nanometric topography. Together, these analyses relate deposit geometry, nucleation-site localization, morphological feature-space organization, route reproducibility, and nanoscale surface relief to the pre-drying state of the protein matrix. We test the hypothesis that the final deposit geometry depends on the physicochemical history accumulated by the protein matrix before the hygrometric transition, including evaporation-driven concentration and time-dependent structural evolution.

## 2. Experimental Details

### *2.1. Protein-Salt Solutions Preparation*

Human serum albumin (HSA) was obtained as a commercial concentrated solution (HIBUMIN®, 20%, Takeda, Austria AG, Vienna, Austria). A 10 wt% NaCl stock solution was prepared by dissolving analytical-grade sodium chloride in deionized water. The protein–salt solutions used for droplet deposition were prepared by volumetric dilution of the HSA solution and the NaCl stock solution with deionized water to obtain final concentrations of 1% HSA and 1 wt% NaCl. All solutions were allowed to stand at room temperature ($22 \pm 1\,^{\circ}\mathrm{C}$) for 30 min before droplet deposition onto the substrate.

### *2.2. Drying of Droplets*

Pattern formation was investigated through the controlled drying of protein solution droplets deposited on polymethyl methacrylate (PMMA) substrates. Droplets were generated using a micropipette to ensure volumetric accuracy, and three droplets of 3 µL were deposited on each microscope slide. This procedure was systematically repeated under identical experimental conditions to ensure statistical reproducibility of the results and to minimize effects associated with local substrate heterogeneities.

Drying was performed using a two-stage hygrometric protocol that separated matrix aging from the final evaporation trigger. The ambient vapor partial pressure was indirectly controlled through regulation of the relative humidity (RH) within a confined system, which is thermodynamically determined by the water activity of the medium according to the relation $P_{\mathrm{amb}} = a_w P_{\mathrm{sat}}(T)$. The high RH condition (80–88%), corresponding to values of $a_w$ close to unity, was achieved by the controlled introduction of distilled water mist generated by an atomizer, which allowed the vapor partial pressure to be rapidly raised to hygrometric equilibrium within the confined volume. Under these conditions, the droplets were maintained for a defined residence time, $t_r$. Under these conditions, evaporation was attenuated relative to the subsequent low-RH stage but was not suppressed. Time-resolved lateral imaging showed progressive thinning of the droplet during residence at high RH. For the shortest residence condition, the hygrometric transition was induced while the droplet still retained a curved liquid profile, whereas for longer residence times the matrix

had already reached a macroscopically flattened state before the transition. A schematic of the confinement setup, relative humidity control, and hygrometric transition protocol employed in the experiments is shown in Figure 1.

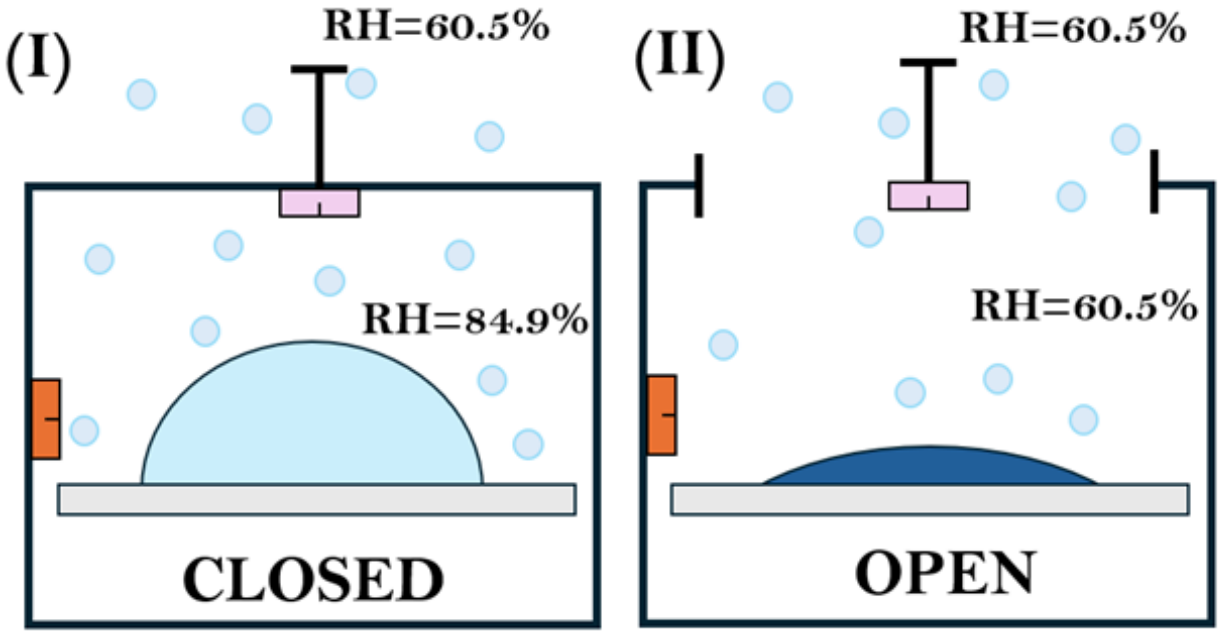



**Figure 1.** Schematic of the hygrometric control protocol employed for pattern formation. (**I**) Protein droplet confined within a closed system under high relative humidity (RH ≈ 84.9%), corresponding to water activity values close to unity, during the controlled residence stage preceding the hygrometric transition. (**II**) Open system after the abrupt induction of the hygrometric transition, with the relative humidity equilibrated to that of the laboratory environment (RH ≈ 60.5%), which generates an increased vapor partial pressure gradient and activates the accelerated evaporation regime leading to the formation of the final deposit. Orange elements indicate digital cameras.

Three characteristic times are used throughout the manuscript. The residence time, $t_r$, is defined as the total time elapsed from droplet deposition ($t = 0$) to the hygrometric transition. The post-gel aging time, $t_g$, corresponds to the interval between the sol–gel transition ($t_{\text{gel}} \approx 240$ min) and the hygrometric transition. Therefore, for post-gel conditions, $t_g = t_r - t_{\text{gel}}$. Finally, the pattern-formation time, $t_p$, is defined as the time elapsed from the hygrometric transition to the appearance of the final pattern.

The hygrometric transition was abruptly induced by the controlled opening of the confined system, exposing the samples to the laboratory atmosphere. This procedure produced a discontinuous decrease in $a_w$ and, consequently, in the vapor partial pressure of the droplet environment, thereby increasing the evaporative driving force. The humidity drop therefore acted as a reproducible trigger applied at different stages of the preceding high-RH evolution of the sample. The temporal reproducibility of this transition, as well as the associated drop in vapor partial pressure, was experimentally verified and is documented in the Supplementary Material.

### *2.3. Acquisition of Photographic and AFM Images*

The drying dynamics and pattern formation were simultaneously recorded from two complementary observation geometries. The frontal evolution of the droplet was acquired by digital microscopy in a configuration normal to the substrate plane, which enabled real time monitoring of the emergence and development of the internal structures associated with nucleation and aggregate growth processes. In parallel, the lateral evolution was recorded using a second digital microscopy system arranged in a tangential configuration,

in order to quantify the temporal variation of the axial profile, the volumetric contraction, and the thinning kinetics of the droplet during drying. Synchronized acquisition allowed us to relate droplet-shape evolution to the onset and progression of internal pattern formation. For optical morphometric analyses, 59, 61, 77, 59, and 66 independent dried droplets were analyzed for residence times of 3, 4, 6, 24, and 72 h, respectively.

## 3. Image Analysis

### *3.1. Image Analysis and Morphological Quantification*

All images of the dried droplet deposits were processed using a dedicated computational pipeline, specifically developed for this study in a *Python 3.10.11* environment and executed under a fixed software configuration to ensure numerical reproducibility across all datasets. The workflow combines geometrically constrained segmentation, polar-coordinate normalization, multiscale feature extraction, and unsupervised clustering to obtain a reproducible and physically interpretable characterization of the internal morphogenetic organization of the protein deposits.

### *3.2. Preprocessing and Spatial Normalization*

Raw grayscale images were converted into floating-point intensity maps and normalized within the interval $[0, 1]$. When required, illumination inhomogeneities were corrected using a rolling-ball type normalization procedure implemented through large–kernel Gaussian filtering. Droplet segmentation was performed using a geometrically constrained approach in which the droplet center was explicitly forced to coincide with the image center, enforcing a strictly consistent radial reference across all samples. The effective droplet radius was defined as a fixed fraction (typically 93%) of the minimum image dimension, followed by mild morphological erosion to remove boundary artifacts and contact-line irregularities, independently of peripheral contrast fluctuations. Once segmented, each image was transformed from Cartesian to normalized polar coordinates. This transformation generates a two–dimensional representation defined over the radial and angular dimensions with fixed resolution (typically 240 radial bins $\times$ 360 angular sectors), converting radial growth and angular branching into rectilinear structures amenable to statistical analysis. The binary droplet mask was transformed identically to preserve exact spatial correspondence and to exclude external background contributions. To enable localized regional analysis, the polar domain was subdivided into a structured grid of radial bands and angular sectors, generating a uniform set of polar ROIs. Each ROI was filtered according to its fractional occupancy within the droplet mask, retaining only those regions exceeding a minimum coverage threshold (typically 60%), thus ensuring statistical validity of the computed descriptors.

### *3.3. Multiscale Morphophysical Descriptors*

Each deposit was quantified using descriptors sensitive to texture, ridge topology, branch orientation, and radial organization. Gray Level Cooccurrence Matrices (GLCMs) were computed from polar images quantized to 64 gray levels, considering multiple pixel distances and angular orientations. From these matrices, reduced texture descriptors including mean contrast, homogeneity, and entropy were extracted as quantitative measures of radial heterogeneity and directional organization.

In parallel, the global Shannon entropy of the polar intensity distribution was computed as an information theoretic measure of overall morphological disorder. This parameter was used exclusively for diagnostic and reporting purposes and was not incorporated into the feature vector used for clustering. Multiscale ridge enhancement was performed using the Sato vesselness filter applied over multiple spatial scales. High-response ridge pix-

els were thresholded using adaptive quantiles and topologically refined via skeletonization. From the resulting skeleton network, normalized descriptors were computed, including total skeleton length, endpoint density, junction density, and the circular standard deviation of branch orientations, describing the topological complexity and orientational organization of the dendritic network.

Local orientational coherence was evaluated using the structure tensor formalism at multiple Gaussian smoothing scales. The coherence metric, defined from the eigenvalue contrast of the tensor field, quantifies directional anisotropy and spatial alignment of dendritic features. The mean value and standard deviation of the coherence field were retained as scalar descriptors. In addition, a probabilistic Hough transform was applied to edge maps in the polar domain to identify long linear structures associated with dominant dendritic trunks. From these detections, the number of segments, total normalized length, maximum segment length, and angular dispersion were extracted as metrics of long range morphological directionality. All feature families were standardized using $z$-score normalization and merged into a single high-dimensional feature vector for each sample. Subsequently, per-sample L2 normalization was applied to ensure metric consistency for clustering analyses.

### *3.4. Unsupervised Classification and Morphological Feature-Space Projection*

The normalized feature matrix was subjected to unsupervised classification using Gaussian Mixture Models (GMMs) with tied covariance structure. The number of clusters was systematically explored within a predefined range (typically $k = 2$–15), and model quality was evaluated using the Silhouette coefficient (cosine metric) and the Davies–Bouldin index. Candidate cluster solutions were compared using Silhouette and Davies–Bouldin metrics. The selected value of k was the smallest solution that preserved morphologically distinguishable groups without fragmenting visually similar deposits. For the selected clustering configuration, posterior membership probabilities were computed for each sample. In parallel, a three-dimensional Principal Component Analysis (PCA) was independently performed for each residence-time dataset using the standardized descriptor space. The first three principal components were retained for visualization, and their explained variance ratios are reported in Figure 4.

### *3.5. Confidence Index and Data Export*

An adaptive confidence index was assigned to the final clustering solution by combining normalized Silhouette and Davies–Bouldin scores with configurable weighting factors. This index was used as an internal diagnostic of cluster separation and compactness. Final results, including morphological features, posterior probabilities, cluster assignments, and validation metrics, were exported in structured Excel files to ensure traceability and downstream quantitative analysis.

Figure 2 summarizes the image-processing workflow used to segment the deposits, transform them into polar coordinates, extract morphophysical descriptors, and classify the resulting feature space.

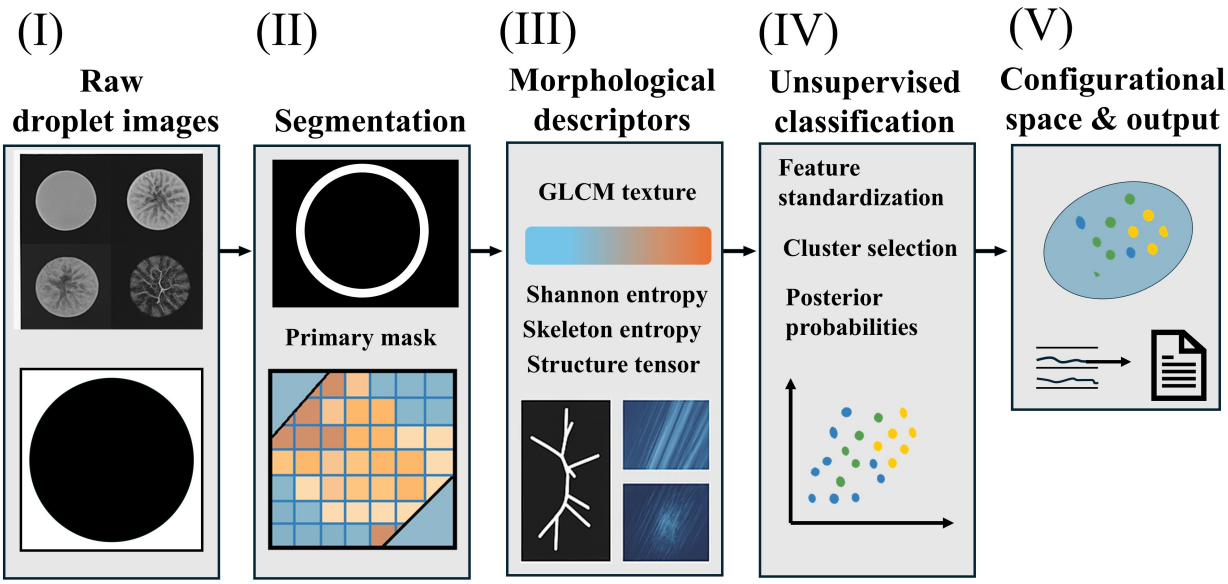



**Figure 2.** Multiscale morphophysical pipeline for residence-time-dependent pattern formation. Raw droplet images are geometrically segmented, mapped into normalized polar coordinates, and processed to extract multiscale texture, topological and directional descriptors. The integrated feature space is classified by Gaussian mixture models, and condition-specific PCA projections visualize the internal organization of the descriptor space for each residence-time dataset.

## 4. Results

The comparative analysis of the morphologies obtained under different residence times ($t_r$), defined as the total time elapsed from $t = 0$ to the hygrometric transition, reveals a systematic trend in the spatial organization of the HSA deposits. Figure 3 compares ten representative deposits corresponding to three well-defined experimental regimes: (i) a pre-gel condition (3 h), in which the droplet remains entirely in the liquid phase before the hygrometric transition; (ii) two early gelation conditions (4 h and 6 h), associated with times immediately after the sol–gel transition threshold (≈240 min); and (iii) two prolonged-residence conditions (24 h and 72 h), corresponding to samples maintained under high relative humidity for substantially longer intervals after the gelation threshold.

Visual inspection of the deposits reveals clear differences in the internal organization of the patterns before and immediately after the gelation threshold. In particular, shorter $t_r$ values are consistently associated with increased morphological heterogeneity, reflected in more dispersed patterns and a higher variability in the spatial organization of the deposits. At 3 h, the deposits exhibit highly variable configurations, with irregularly oriented branched domains, interspersed amorphous regions, and a markedly heterogeneous distribution of internal aggregates. In contrast, for the 4 h and 6 h conditions, the patterns display more clearly defined branches and an increased geometric coherence relative to the 3 h set, although appreciable variations in the number, orientation, and extent of the main dendrites still persist among replicates. For prolonged residence times (≥24 h), the internal organization becomes markedly more uniform. The dendrites exhibit coherent and reproducible orientations, with well-defined principal axes and an internal geometry that repeats with only minor variations between samples. For both the 24 h and 72 h conditions, the number of distinct configurations decreases noticeably, converging into one or two dominant patterns within each experimental set. This decrease in visual diversity motivated the subsequent quantitative discrimination based on texture descriptors.




**Figure 3.** Representative dried HSA deposits obtained under different residence times ($t_r$). $t_r$: pre–gel condition (3 h), conditions at and shortly after the gelation threshold (4 and 6 h), and prolonged-residence conditions (24 and 72 h). A systematic transition is observed from highly heterogeneous, dispersed patterns at short residence times to coherent and reproducible dendritic architectures at prolonged residence times.

To assess the internal organization of the quantitative descriptor space, PCA was applied independently to each residence-time dataset using the same multiscale descriptor set that includes GLCM metrics, morphological skeleton parameters, directional coherence derived from the tensor structure, and radial descriptors computed in polar coordinates. The partitions generated by the Gaussian mixture model were subsequently examined for different values of $k$. Figure 4 shows the condition-specific projections of the samples onto independently fitted PCA spaces, allowing the internal group structure of each residence-time dataset to be examined separately. The GMM centroids fell on the densest PCA regions, supporting that the clusters reflect structure in the data rather than arbitrary partitioning. The first three principal components accounted for 71.45%, 77.39%, 71.32%, 65.62%, and 68.85% of the total variance for the 3, 4, 6, 24, and 72 h datasets, respectively.

The condition-specific PCA projections reveal clear differences in the internal organization of the configurations defined by the GMM. At 3 h, the data points are widely distributed throughout the PCA cloud, without a dominant concentration, reflecting the high structural diversity observed in the original images. At 4 h, although an incipient clustering becomes apparent, the distribution remains broad and is composed of several dispersed subclusters, consistent with the presence of heterogeneous internal aggregates. At 6 h, clearly distinguishable groups emerge together with a low-frequency residual set, indicating a transition toward more recurrent patterns, although appreciable inter-sample variability is still present.

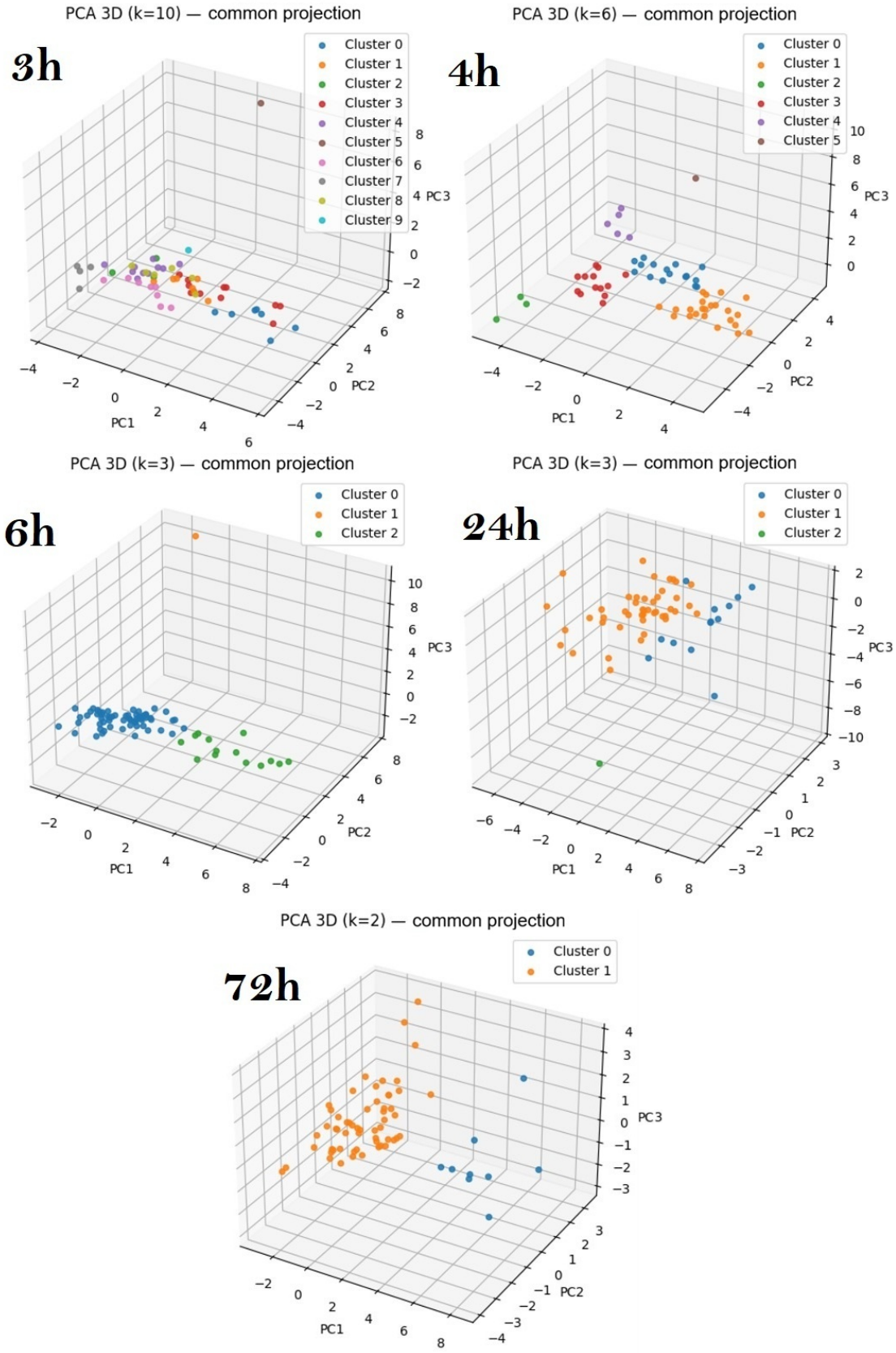



**Figure 4.** Independent three-dimensional PCA projections for each residence-time dataset. The explained variance of PC1, PC2, and PC3 is indicated on the corresponding axes, and colors denote the GMM-defined morphotypes.

For prolonged residence times, the PCA projections show a more clearly defined internal organization of the morphological configurations. At 24 h, the deposits are organized into differentiated domains of the latent space, in agreement with the morphological stabilization previously described by visual inspection. This behavior becomes more evident at 72 h, when the data are organized into well-defined groups, with one of them clearly predominant. In parallel, the morphotype distribution determined by the GMM shows a progressive reduction in morphological diversity and a greater recurrence of specific structural configurations. Altogether, the condition-specific projections show distinct internal organizations within each independently fitted PCA space: short-residence datasets contain multiple distributed subgroups, whereas prolonged-residence datasets contain recurrent, clearly differentiated groups. These observations are interpreted together with the GMM morphotype frequencies; the absolute extent or dispersion of different PCA clouds is not compared across residence times.

Figure 5 shows that the classification of the patterns exhibits marked differences in the relative frequency of morphotypes as the residence time $t_r$ varies. At 3 h, the deposits are distributed almost uniformly among ten distinct configurations, without a predominant motif, in agreement with the high structural heterogeneity identified in the original images. At 4 h, the number of morphotypes decreases and the distribution becomes non-uniform: a dominant pattern emerges, followed by several minor configurations, reflecting the onset of convergence toward more ordered patterns. This trend intensifies at 6 h, where only three morphotypes are detected by the classifier, one of them accounting for most of the samples. These variations in occurrence probability indicate that, in the intervals preceding and immediately following gelation, the droplets still explore a broad morphospace, although a reduction in diversity already becomes evident. For prolonged residence times, the morphotype distribution becomes even more compact and is dominated by one or two main patterns. At 24 h, three configurations suffice to describe the entire dataset, with one clearly predominant morphotype and two low-frequency variants, consistent with the reduced morphological diversity observed in the PCA projections. This reduction in the pattern repertoire reaches its maximum expression at 72 h, where only two morphotypes appear in the samples, one of them representing nearly the totality of the deposits. The circular summary shows the same trend: long residence times are associated with a narrower and more reproducible set of morphologies.

Figure 6 shows that the images obtained by atomic force microscopy (AFM) enable nanometric-resolution characterization of the topography associated with the most representative morphotypes at each residence time. For the 3 h condition, the second most frequent configuration ($D3_2$) was analyzed. This choice is justified by its topological proximity within the PCA space to the dominant variants ($D3_1$, $D3_2$, and $D3_3$), such that its relief reliably captures the most characteristic structural features emerging in droplets subjected to a hygrometric transition prior to gelation. The AFM maps reveal a surface composed of dispersed micro-islands, isolated peaks, and regions of incomplete interconnection between units, reflecting a deposit still governed by heterogeneous material compaction and by local aggregation processes characteristic of the earliest stages of evaporation. At 6 h, the topography exhibits more continuous ridges and better-defined depressions, with a set of structural units that is more coherent than at early times. At 72 h, the dominant morphotypes display well-delineated repetitive aggregates, with broad ridges, low-roughness regions, and an internal organization that is highly reproducible across samples, showing increased recurrence of the observed topographic organization. Although the vertical scale is kept constant across all three residence times, the relief architecture evolves from dispersed microstructures at 3 h to well-defined and persistently reproduced patterns at 72 h.

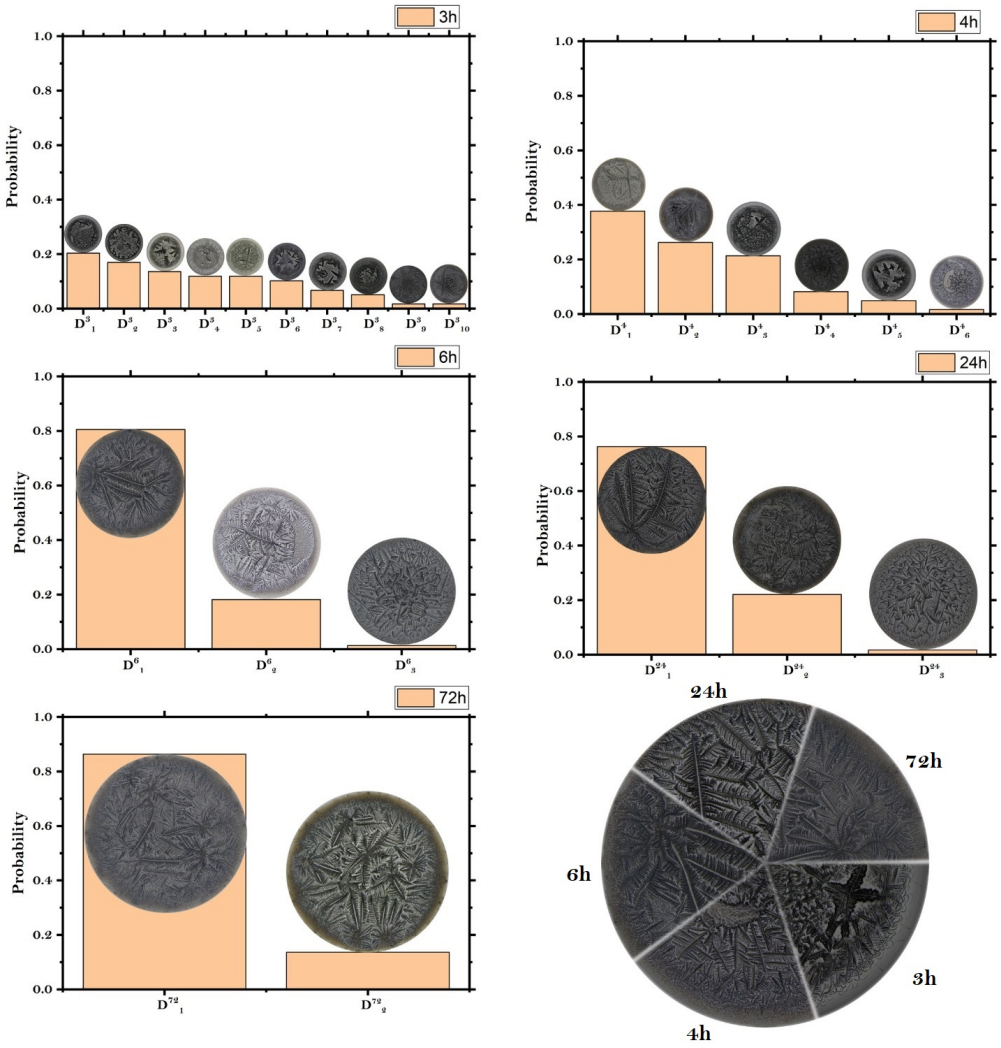



**Figure 5.** Relative frequency and sample counts ($n$) of GMM-identified morphotypes for each residence time. Total sample sizes were $N = 59, 61, 77, 59$, and 66 for 3, 4, 6, 24, and 72 h, respectively.

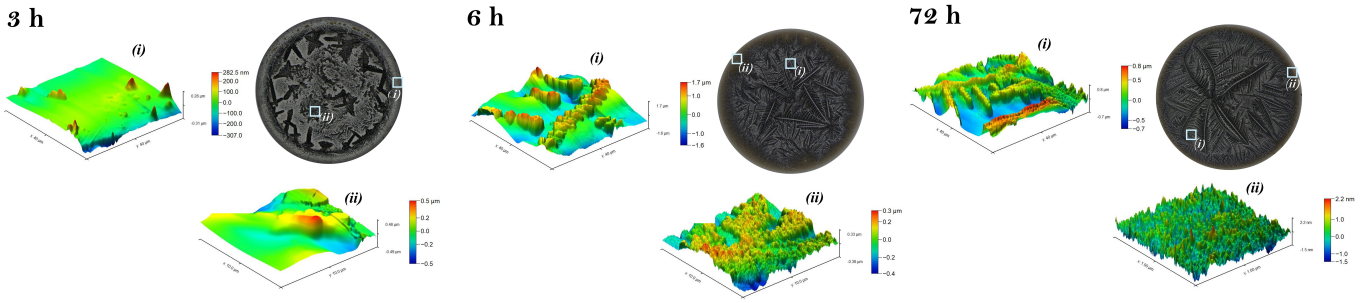



**Figure 6.** Representative AFM topographies of characteristic morphotype at 3 h, 6 h, and 72 h. Surface architecture evolves from dispersed micro-islands and incomplete aggregation to well-defined, repetitive structures with recurrent topographic organization at prolonged residence.

Quantitative analysis of the AFM topographies confirms that the surface evolution does not correspond to a monotonic decrease in roughness, but rather to a multiscale reorganization of the surface relief. The root mean square height roughness ($S_q$), skewness ($S_{sk}$), excess kurtosis ($K_{\text{excess}}$), and correlation lengths are summarized in Table 1. For maps acquired at the common scale of 40 × 40 μm$^2$, $S_q$ changes from 49.23 nm at 3 h to 551.6 nm at 6 h and subsequently decreases to 291.3 nm at 72 h. This evolution indicates

a transient increase in the vertical amplitude of the surface relief during the intermediate regime, followed by a partial reduction after prolonged residence. The concomitant variations in $S_{sk}$ and $K_{\text{excess}}$ show that this evolution is not restricted to the amplitude of the height fluctuations, but also involves changes in the statistical organization of the height distribution.

**Table 1.** Quantitative AFM descriptors obtained from the representative topographic regions at different residence times. $S_q$ is the root mean square height roughness, $S_{sk}$ is the height-distribution skewness, and $K_{\text{excess}}$ is the excess kurtosis. $T_H$ and $T_V$ denote the horizontal and vertical correlation lengths, respectively, calculated from the decay of the corrected autocorrelation function to $1/e$.

| $t_r$ | Region | Scan Size (μm$^2$) | $S_q$ (nm) | $S_{sk}$ | $K_{\text{excess}}$ | $T_H$ (μm) | $T_V$ (μm) |
|---|---|---|---|---|---|---|---|
| 3 h | (i) | $10 \times 10$ | 128.2 | 0.229 | 0.745 | 1.788 | 2.253 |
| 3 h | (ii) | $40 \times 40$ | 49.23 | −0.575 | 4.436 | 5.390 | 2.221 |
| 6 h | (i) | $40 \times 40$ | 551.6 | 0.471 | −0.472 | 3.767 | 3.616 |
| 6 h | (ii) | $10 \times 10$ | 115.6 | −0.428 | −0.315 | 0.944 | 1.188 |
| 72 h | (i) | $40 \times 40$ | 291.3 | 0.387 | −0.615 | 2.771 | 3.092 |
| 72 h | (ii) | $1 \times 1$ | 0.4051 | 0.215 | 0.444 | 0.02095 | 0.02407 |

The correlation lengths further reveal changes in the lateral organization of the surface structures. In region (ii) at 3 h, the horizontal and vertical correlation lengths are 5.390 and 2.221 μm, respectively, indicating a pronounced directional dependence. In contrast, region (i) at 6 h exhibits comparable values of 3.767 and 3.616 μm, while values of 2.771 and 3.092 μm are obtained at 72 h, indicating a more comparable lateral persistence along both directions. At the local scale of $1 \times 1$ μm$^2$, region (ii) at 72 h exhibits $S_q = 0.4051$ nm and horizontal and vertical correlation lengths of 20.95 and 24.07 nm, respectively, identifying locally smooth domains with a nanometric lateral organization scale. Because the lateral scan sizes range from 1 to 40 μm, these quantities are interpreted as local topographic descriptors at their corresponding observation scales rather than as directly comparable measures of the global roughness of the deposit.

*Pattern Formation*

The pattern-formation sequences show a systematic dependence on the residence time, $t_r$, before the hygrometric transition. Figure 7a shows that during the first 180 min the droplet retains an optically stable surface and a well-defined curved profile, with no visible evidence of incipient aggregation. When the hygrometric transition is triggered under this pre-gel condition, multiple irregular nuclei emerge at different locations on the substrate, followed by heterogeneous branching without a preferred growth direction. By 187 min, these structures evolve into the final pattern, indicating that under the shortest residence condition the hygrometric transition and pattern formation occur before the gelation threshold is reached.

Figure 7b shows that once the gelation threshold is reached (approximately 240 min), the droplet surface becomes homogeneously opaque, consistent with the formation of a continuous protein-rich matrix on the substrate. From that point onward, the system remains in the gel state for an additional post-gel aging time, $t_g$, before the hygrometric transition is triggered. Under the present experimental conditions, $t_g$ ranges from approximately 1 to 4080 min. The total residence time prior to the hygrometric transition is $t_r = 241$, 360, 1440, and 4320 min, measured from $t = 0$. This post-gel aging interval provides additional time for the protein matrix to evolve before the final drying stage. Within a glassy-relaxation framework, the differences observed between short and prolonged post-gel residence times can be interpreted as reflecting time-dependent evolution of the matrix before the hygro-

metric transition. Such evolution may progressively reduce the number of nucleation sites and growth trajectories available during subsequent pattern formation.

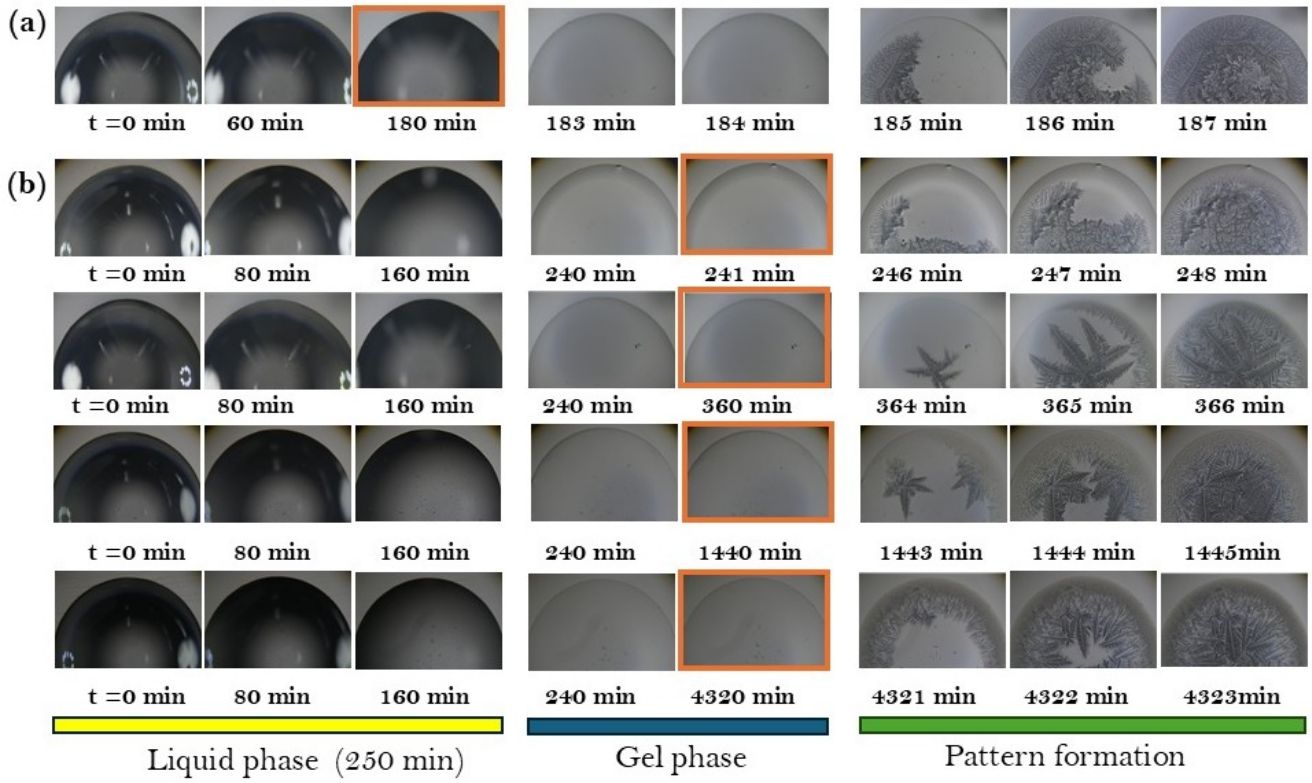



**Figure 7.** Time-resolved pattern formation following the hygrometric transition. (**a**) Transition applied in the pre-gel state, leading to distributed multi-site nucleation and heterogeneous growth. (**b**) Transition applied after gelation, showing the residence-time dependence of nucleation and dendritic organization. Time labels within each sequence denote the elapsed experimental time, $t$, measured from droplet deposition. Orange boxes indicate the instant at which the hygrometric transition is triggered, corresponding to $t = t_r$. The colored bars at the bottom denote the dominant experimental regimes: yellow corresponds to the pre-gel stage, blue to the post-gel residence stage under high relative humidity, and green to the pattern-formation stage following the hygrometric transition.

The temporal sequences shown in Figure 7b illustrate how different residence times are associated with distinct nucleation regimes. When the hygrometric transition is triggered at $t_r = 241$ min, the deposit remains nearly homogeneous during the first minutes and aggregates appear abruptly, with several thin branches growing from different points along the perimeter. When the hygrometric transition is triggered at $t_r = 360$ min (6 h), pattern formation initiates from a reduced number of nuclei, preferentially located in the mid-region of the deposit. The branches become thicker and tend to bifurcate along similar directions across samples. Unlike the previous case, the droplet interior already displays a recognizable network with regions in which branches compete for space, conferring a higher degree of organization to the pattern.

When the hygrometric transition is triggered at $t_r = 1440$ min (24 h), the appearance of aggregates is practically immediate after the humidity drop. The pattern develops from a few well-defined nucleation centers, and the main branches grow in a highly similar manner from one sample to another, yielding a reproducible dendritic geometry with nearly uniform thickness and no visible interruptions in structural continuity. When the hygrometric transition is triggered at $t_r = 4320$ min (72 h), branch growth extends with stable morphology and nearly constant thickness from the nucleation sites to the tips. The resulting structure exhibits similar shapes and spatial distributions across samples,

showing that prolonged residence is associated with a more restricted and reproducible set of growth trajectories.

Figure 8 enables a direct comparison between the mode of early nucleus emergence and the subsequent development of dendritic growth under two strongly contrasting residence times. For droplets with $t_r = 3$ h, nucleation occurs in a spatially distributed manner at multiple locations across the deposit, without any preferred position and with heterogeneous initial geometries. The magnified views (i)–(iv) show representative examples of these early nuclei: some adopt cross-like configurations, others display short branches extending along uncorrelated orientations, and several reach the critical size almost simultaneously. This multiplicity of active centers, mutually separated and lacking a dominant growth direction, leads to a final pattern composed of independent aggregates with heterogeneous growth trajectories.

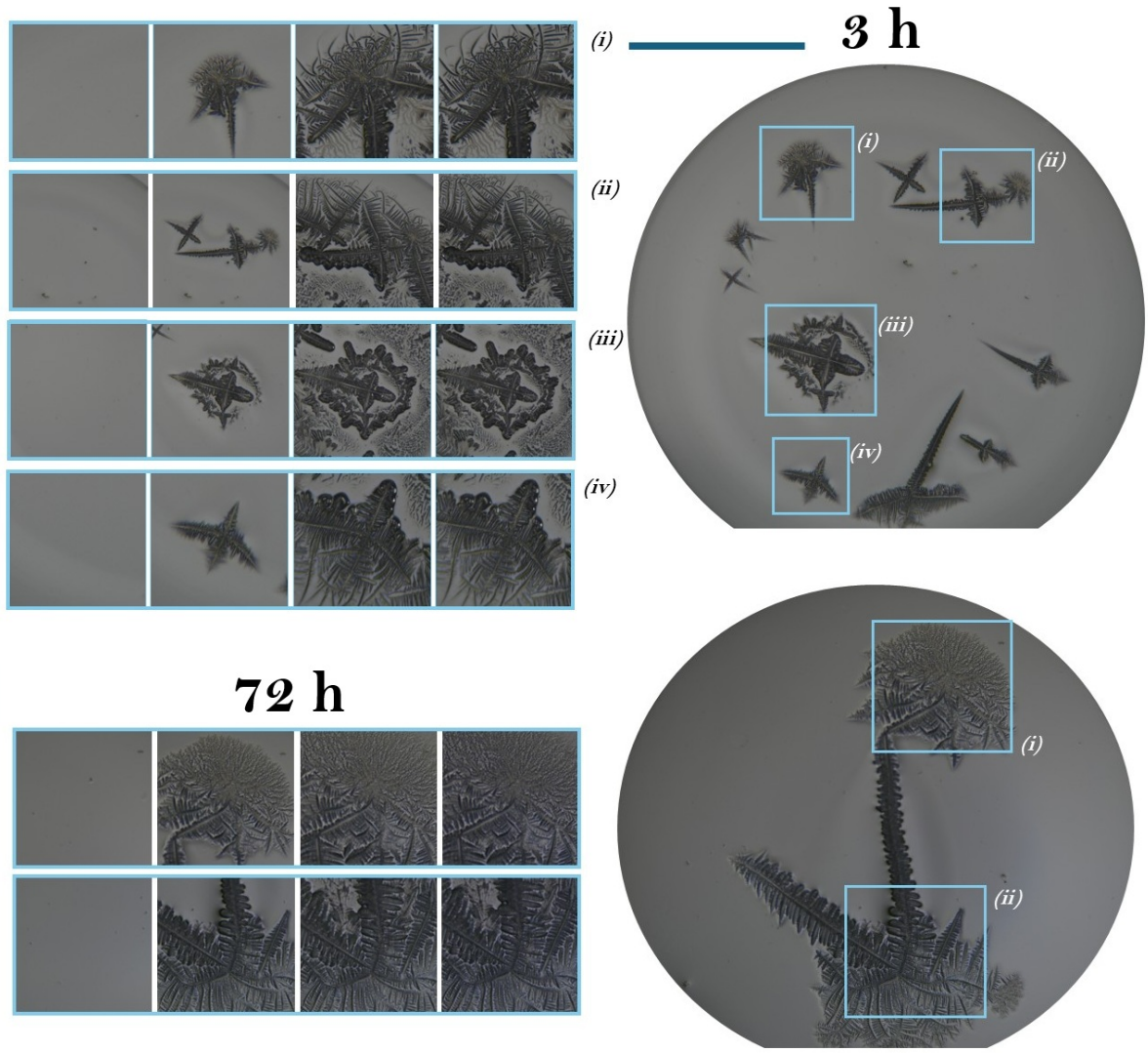



**Figure 8.** Direct comparison of nucleation and dendritic growth for $t_r = 3$ h and $t_r = 72$ h. At 3 h, nucleation is spatially distributed and competitive, leading to disconnected aggregates. At 72 h, nucleation is restricted to a few dominant sites, producing highly reproducible dendritic patterns.

In contrast, droplets with $t_r = 72$ h exhibit a completely different nucleation regime. The magnifications show that the primary nuclei localize at a very small number of sites, which are invariant across replicates, and rapidly evolve into highly stable branched structures. Growth proceeds from a few dominant centers, with thick branches, nearly

constant bifurcation angles, and spatial continuity spanning large regions of the deposit. Unlike the 3 h case, inter-branch competition is minimal, and the complete pattern adopts a highly reproducible organization. The reduced number of nuclei and the reproducible branching directions at 72 h show that prolonged residence is associated with a narrower set of nucleation events and subsequent growth trajectories. The residence-time dependence of the nucleation mode observed in Figure 8 is consistent with changes in the state of the protein matrix before the hygrometric transition and is accompanied by a corresponding change in the temporal scale of pattern formation. This residence-time dependence of pattern-formation kinetics is summarized in Figure 9.

Figure 9 shows that the time required for the final pattern to emerge after the hygrometric transition, $t_p$, decreases as $t_r$ increases. The strongest reduction occurs between $t_r = 3$ h and $t_r = 4$ h, reflecting the shift from a pre-gel droplet to a system that has already entered the gel state at the moment of humidity reduction. Under these early conditions, several minutes are required for nucleation and growth to stabilize. Once the transition is applied after the gelation threshold, $t_p$ decreases sharply and remains within a narrower interval. At $t_r = 72$ h, $t_p$ reaches its minimum value, showing that prolonged residence is associated with nearly immediate pattern growth upon humidity reduction.

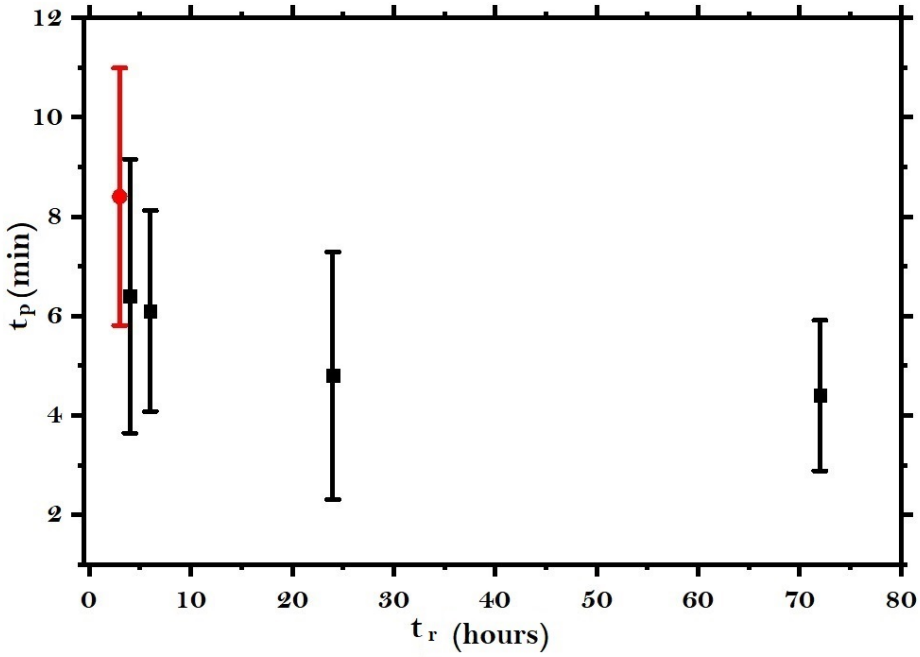



**Figure 9.** Dependence of the pattern appearance time $t_p$ on the residence time $t_r$. Points represent mean values obtained from $n = 10$ droplets per condition; error bars indicate one standard deviation. The number of independent experimental replicates could not be established retrospectively. The red marker and error bar indicate the pre-gel condition at the onset of the hygrometric transition ($t_r = 3$ h).

Figure 10 compares the normalized axial profiles, $h/h_0$, recorded during the high-RH residence stage for representative residence-time conditions. The profiles follow similar early thinning trajectories, showing progressive reduction of the droplet height under high RH. For the shortest residence condition ($t_r \approx 3$ h), the hygrometric transition occurs while the droplet still retains a finite curved profile. In contrast, for the longer residence conditions, the sample reaches a macroscopically flattened profile before the hygrometric transition is applied. Thus, solvent loss and the associated concentration of the nonvolatile components occur during the residence stage and cannot be considered negligible. However, the normalized optical profiles do not resolve possible residual solvent loss after

macroscopic flattening; therefore, additional slow concentration changes during prolonged residence cannot be excluded.

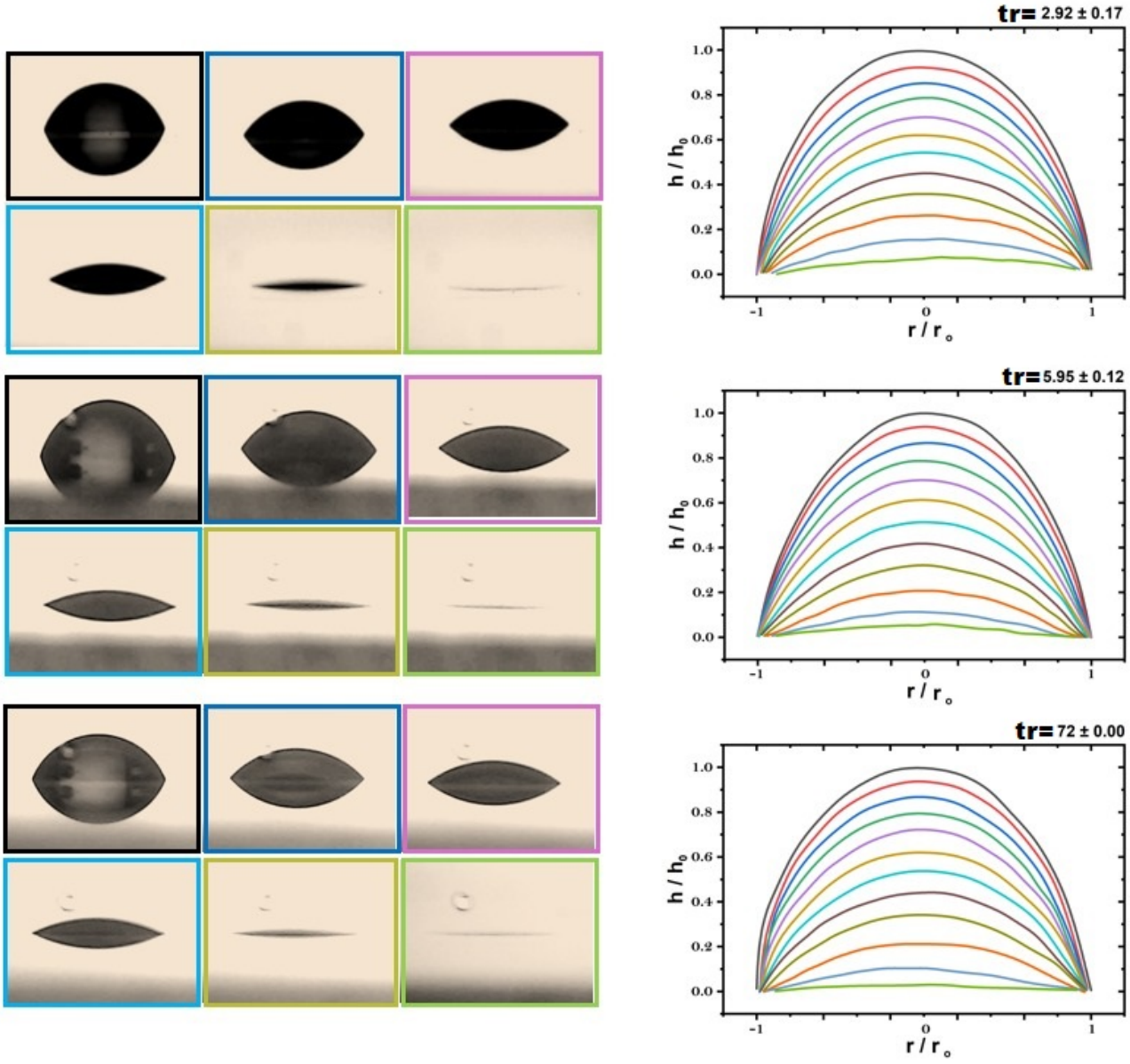



**Figure 10.** Normalized axial profiles $h/h_0$ during the high-RH residence stage for representative residence-time conditions. (**Upper**, **middle**, and **lower**) panels correspond to $t_r = 2.92 \pm 0.17$ h, $5.95 \pm 0.12$ h, and 72 h, respectively. Successive profiles were extracted at 20 min intervals starting from droplet deposition; in the (**upper**) panel, the last two profiles correspond to 181 and 184 min, whereas in the (**middle** and **lower**) panels the last profiles correspond to 200 and 220 min. The black, blue, purple, cyan, olive, and light green borders match the colors of the corresponding curves in the plots on the right, which show successive stages in the temporal evolution of the droplet profiles. In the (**middle** and **lower**) panels, the hygrometric transition was applied after the last recorded profile, once the sample had already reached a macroscopically flattened state. These normalized profiles characterize the macroscopic thinning stage but do not exclude residual solvent loss after flattening.

The mechanistic scheme summarized in Figure 11 integrates the structural, dynamical, and morphological levels of the system and illustrates a proposed relationship between the pre-transition evolution of the protein matrix, the nucleation pathways expressed after the hygrometric transition, and the final geometry of the deposit. In the upper band,

the progression from short to prolonged residence illustrates the proposed mechanistic interpretation that time-dependent evolution of the gel matrix progressively restricts the set of structural rearrangement pathways available before the hygrometric transition. This proposed restriction is represented in the second band as a progressive reduction in the set of nucleation trajectories, evolving from multiple divergent routes at short residence times toward a narrower set of recurrent growth pathways after prolonged residence. In the lower band, the corresponding evolution of the final deposit morphology is represented by irregular aggregates and disordered branching at short residence times, partially coherent dendrites at intermediate conditions, and thick, continuous, highly reproducible structures after prolonged residence. Taken together, these correspondences support a mechanistic interpretation linking residence-time-dependent matrix evolution with nucleation behavior and final pattern geometry. The configurational and free-energy landscapes represented by this scheme are conceptual and were not directly measured.

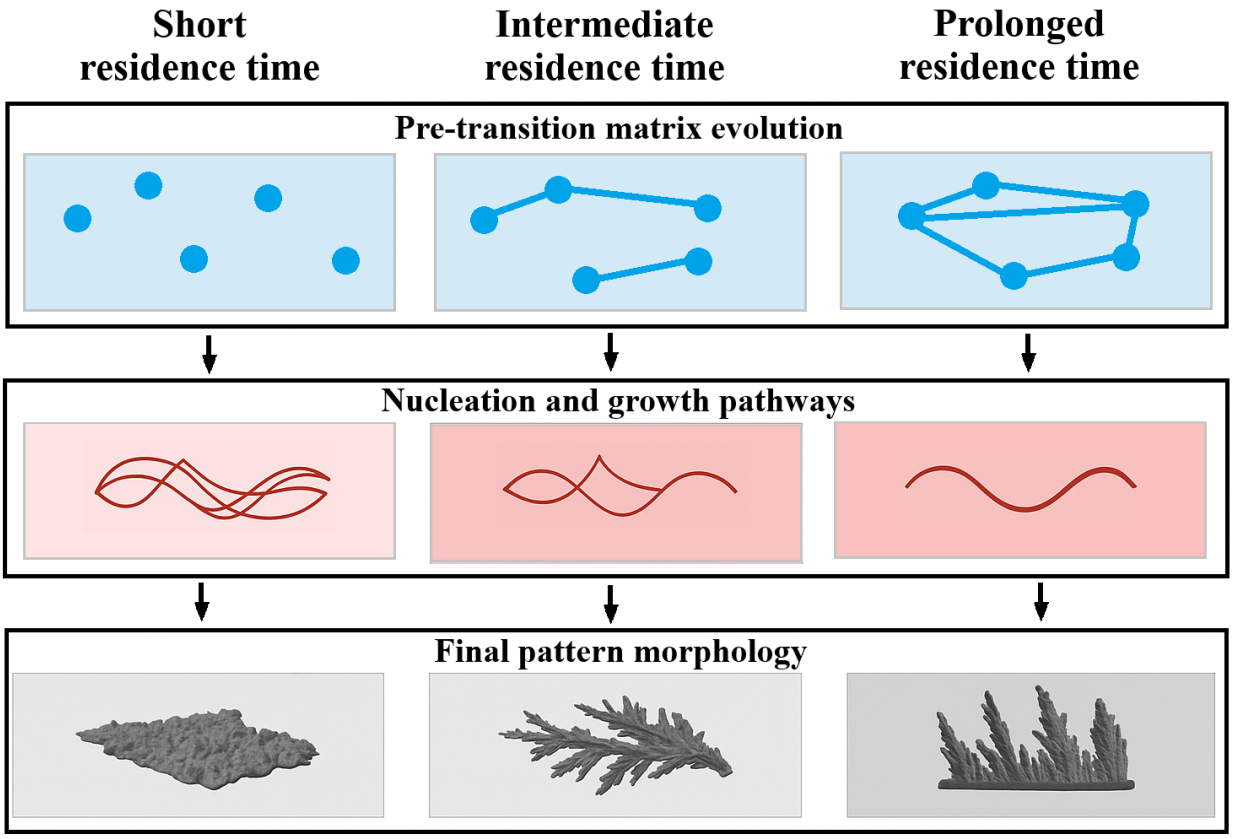



**Figure 11.** Conceptual mechanistic scheme linking residence-time-dependent matrix evolution, nucleation pathways, and final pattern morphology. Prolonged residence is associated with a progressive restriction of the observed nucleation and growth pathways and with increasingly reproducible dendritic architectures. The proposed evolution of the gel state represents a mechanistic interpretation rather than a directly measured configurational or free-energy landscape.

## 5. Discussion

The results indicate that the residence time, $t_r$, before the hygrometric transition is associated with systematic changes in the architecture of the final deposit. These observations support the interpretation that morphological diversity depends on the physicochemical state reached by the matrix before the humidity drop and cannot be attributed solely to the subsequent drying stage. Together, morphological classification, PCA projections, dendritic organization, and AFM topography are consistent with time-dependent structural evolution

of the gelled matrix during residence under high RH. However, residual mobility, network connectivity, and configurational relaxation were not measured directly and are therefore treated here as mechanistic interpretations of the observed residence-time dependence.

The data distinguish two main morphogenetic regimes associated with the residence time, $t_r$, before the hygrometric transition. In the short-residence regime, multiple competing nucleation events occur simultaneously at spatially distributed locations, with no clearly dominant growth route. These events exhibit heterogeneous initial geometries and early competition among active centers, producing irregular and poorly reproducible branched deposits. The heterogeneous organization observed within the short-residence PCA projection, together with the nearly uniform distribution among multiple morphotypes, is consistent with greater morphological diversity under short-residence conditions.

The second regime is observed at prolonged residence times in the gel phase. Under these conditions, nucleation becomes spatially localized, with only a small number of sites repeatedly activated at comparable positions across replicates. As a consequence, dendritic growth becomes highly reproducible, with thick, continuous branches and similar bifurcation geometries. The condition-specific PCA projections show more recurrent internal organizations, while one or two morphotypes dominate the long-residence datasets. These observations indicate a progressive reduction in the diversity of expressed nucleation and growth pathways and are consistent with a more organized pre-transition matrix state after prolonged residence.

Between these two extremes, an intermediate regime is observed at residence times immediately after the gelation threshold. The partial reduction in morphological diversity, the emergence of incipient PCA clusters, and the decrease in the number of morphotypes indicate a progressive restriction of the expressed nucleation and growth pathways. Within a physical-aging framework, these changes are consistent with gradual structural reorganization of the matrix during residence under high RH. Metastable states and the underlying free-energy landscape were not measured directly and are therefore invoked only as a conceptual interpretation of the observed morphological evolution.

AFM provides complementary evidence of residence-time-dependent changes in surface topography. At short residence times, the surfaces are characterized by microislands, isolated peaks, and incompletely interconnected regions. At intermediate times, more continuous ridges and increased lateral organization become apparent. At long residence times, broad ridges and recurrent topographic motifs dominate the analyzed regions. These observations are consistent with progressive changes in the organization of the protein-rich matrix during residence under high RH. However, AFM characterizes the final surface relief and does not directly measure network connectivity, molecular mobility, configurational relaxation, or metastable states.

The lateral-profile measurements show that solvent loss occurs during the high-RH residence stage. Although the early normalized thinning trajectories are similar across representative conditions, the hygrometric transition is applied at different stages of this evolution. At the shortest residence time, the transition occurs while the droplet retains a curved profile, whereas at longer residence times it occurs after the sample has become macroscopically flattened. Consequently, cumulative solvent loss and the associated increase in effective HSA and NaCl concentrations may contribute to the evolution during $t_r$. Because residual solvent loss after macroscopic flattening was not independently quantified, its contribution cannot be separated from the concurrent time-dependent evolution of the protein matrix. The final patterns should therefore be interpreted as reflecting the physicochemical history accumulated under high RH rather than structural relaxation alone.

The relationship between $t_r$ and the pattern-formation time, $t_p$, further supports a residence-time-dependent change in nucleation kinetics. At short residence times, several

minutes are required for the final pattern to emerge, consistent with the distributed character of the active nucleation sites and early branch competition. In contrast, after prolonged residence, pattern emergence is nearly immediate. This behavior is consistent with the hypothesis that the pre-transition state of the matrix influences the nucleation and growth pathways activated after the humidity drop, although the underlying relaxation dynamics were not measured directly.

A qualitative nucleation framework provides a possible interpretation of these observations. The hygrometric transition increases the evaporative driving force and therefore promotes further solvent removal and local enrichment of the nonvolatile components. In a classical nucleation picture, the thermodynamic driving force increases with supersaturation, $S$, through $\Delta\mu \sim k_{\mathrm{B}}T \ln S$, and the nucleation barrier decreases as the magnitude of this driving force increases. Thus, residence-time-dependent differences in concentration history and in the pre-transition organization of the matrix may modify both the number and spatial distribution of sites from which aggregation or dendritic growth is initiated after the humidity drop. However, supersaturation, solubility, interfacial free energy, critical nucleus size, and nucleation barriers were not measured in the present experiments. Accordingly, classical nucleation theory is invoked here only as a qualitative framework for interpreting the observed changes in nucleation-site number and localization, rather than as a quantitative description of the process.

Although the results show consistent residence-time-dependent trends across techniques and scales, several limitations must be considered. The analysis is restricted to a single protein system and a single hygrometric transition protocol; therefore, the generality of the observed transition between heterogeneous and highly reproducible morphologies cannot yet be established for other biomacromolecules or humidity-drop conditions. In addition, residual solvent loss after macroscopic flattening was not independently quantified, preventing a complete separation between concentration changes and the concurrent time-dependent evolution of the protein matrix during prolonged residence under high RH. Topographic characterization was performed on representative morphotypes rather than on the full set of observed configurations, so finer variations may not be captured by the selected AFM regions. Finally, although PCA and GMM provide a quantitative description of morphological organization and recurrence, they do not directly measure molecular mobility, network connectivity, configurational relaxation, or the underlying free-energy landscape.

Despite these limitations, the data consistently identify residence time as the experimental variable associated with morphological selection in this system. Prolonged residence permits continued physicochemical and structural evolution of the protein matrix before the hygrometric transition, while also encompassing ongoing solvent loss under high RH. Accordingly, $t_r$ should not be interpreted as a direct measure of configurational relaxation. Within the proposed mechanistic framework, the residence-time-dependent evolution of the pre-transition matrix is consistent with the observed reduction in nucleation-site diversity and the increased reproducibility of the final deposits. Controlling $t_r$ may therefore provide a practical route to tune deposit reproducibility and branching geometry in gel-forming systems, with potential relevance to biomedical coatings, controlled deposition, and evaporation-based printing technologies.

## 6. Conclusions

Our results show that the final morphology of these protein deposits is strongly dependent on the residence time before the hygrometric transition. Increasing $t_r$ is associated with a progressive reduction in the diversity of observed nucleation and growth pathways and with increased morphological reproducibility. Short residence times lead to spatially

distributed, competitive nucleation and highly heterogeneous aggregates, whereas long residence times promote highly localized and recurrent nucleation from a reduced number of sites and the formation of coherent, reproducible dendritic architectures.

Time-resolved lateral profiles further show that solvent loss occurs during residence under high RH and may contribute to the physicochemical evolution of the system. Because residual solvent loss after macroscopic flattening was not independently quantified, concentration changes cannot be fully separated from the concurrent time-dependent evolution of the protein matrix. The observed residence-time dependence is nevertheless consistent with a mechanistic picture in which the pre-transition organization of the matrix influences the nucleation and growth pathways activated after the humidity drop. This proposed templating role should be regarded as a mechanistic interpretation rather than a directly demonstrated structural mechanism. Controlling $t_r$ before the hygrometric transition may therefore provide a practical route to tune surface morphology and deposit reproducibility in protein-based and related gel-forming systems.

**Supplementary Materials:** The following supporting information can be downloaded at: https://www.mdpi.com/article/10.3390/fluids11100243/s1, Figure S1: Temporal reproducibility of the hygrometric transition; Figure S2: Morphological consistency of GMM-identified deposit families

**Author Contributions:** H.A.M.-A.: Investigation, Formal analysis, Writing—review & editing; I.G.V.-T.: Formal analysis, Writing—review & editing; O.D.-H.: Formal analysis, Writing—review & editing; H.V.-B.: Formal analysis, Writing—review & editing; Y.J.P.C.: Methodology, Visualization, Writing—review & editing; J.G.-G.: Conceptualization, Resources, Supervision, Project administration, Writing—original draft, Writing—review & editing. All authors have read and agreed to the published version of the manuscript.

**Funding:** This research received no external funding.

**Data Availability Statement:** The data and code that support the findings of this study are available from the corresponding author upon reasonable request.

**Acknowledgments:** H.A.M.-A. acknowledges financial support from SECIHTI fellowships. Y.J.P.C. acknowledges financial support from the SECIHTI postdoctoral fellowship. During the preparation of this work, the authors used ChatGPT (GPT-5.6, OpenAI) solely to improve the English language (grammar, phrasing, and readability). After using the tool, the authors reviewed and edited the text as needed and take full responsibility for the content, including the accuracy and integrity of all parts of the manuscript.

**Conflicts of Interest:** The authors declare no conflicts of interest. The authors declare that they have no known competing financial interests or personal relationships that could have appeared to influence the work reported in this paper.

## References

1. Brutin, D.; Sefiane, K. *Drying of Complex Fluid Drops: Fundamentals and Applications*; Royal Society of Chemistry: Cambridge, UK, 2022.
2. Pal, A.; Gope, A.; Sengupta, A. Drying of bio-colloidal sessile droplets: Advances, applications, and perspectives. *Adv. Colloid Interface Sci.* **2023**, *314*, 102870. [CrossRef] [PubMed]
3. Zang, D.; Tarafdar, S.; Tarasevich, Y.Y.; Choudhury, M.D.; Dutta, T. Evaporation of a Droplet: From physics to applications. *Phys. Rep.* **2019**, *804*, 1–56. [CrossRef]
4. Zhu, G.; Gao, L.; Wang, Y.; Tlusty, T.; Yan, L.T. Programmable Potentials Choreograph Defects in a Colloidal Crystal Shell. *Phys. Rev. Lett.* **2024**, *132*, 048201. [CrossRef] [PubMed]
5. Deegan, R.D. Pattern formation in drying drops. *Phys. Rev. E* **2000**, *61*, 475. [CrossRef] [PubMed]
6. Deegan, R.D.; Bakajin, O.; Dupont, T.F.; Huber, G.; Nagel, S.R.; Witten, T.A. Capillary flow as the cause of ring stains from dried liquid drops. *Nature* **1997**, *389*, 827–829. Correction in *Nature* **2021**, *592*, E12. [CrossRef]
7. Hu, H.; Larson, R.G. Analysis of the microfluid flow in an evaporating sessile droplet. *Langmuir* **2005**, *21*, 3963–3971. [CrossRef] [PubMed]

8. Carreón, Y.J.; Pereyra Zarate, A.A.; Pérez Sánchez, A.E.; Díaz-Hernández, O.; González-Gutiérrez, J. Surface coating with foliar fertilizers. *Coatings* **2024**, *14*, 1007. [CrossRef]
9. Pal, A.; Gope, A.; Athair, A.S.; Iannacchione, G.S. A comparative study of the drying evolution and dried morphology of two globular proteins in de-ionized water solutions. *RSC Adv.* **2020**, *10*, 16906–16916. [CrossRef] [PubMed]
10. Yakhno, T.; Yakhno, V. Structural evolution of drying drops of biological fluids. *Tech. Phys.* **2009**, *54*, 1219–1227. [CrossRef]
11. Gorr, H.M.; Zueger, J.M.; McAdams, D.R.; Barnard, J.A. Salt-induced pattern formation in evaporating droplets of lysozyme solutions. *Colloids Surf. B Biointerfaces* **2013**, *103*, 59–66. [CrossRef] [PubMed]
12. Davies, J.F.; Miles, R.E.; Haddrell, A.E.; Reid, J.P. Temperature dependence of the vapor pressure and evaporation coefficient of supercooled water. *J. Geophys. Res. Atmos.* **2014**, *119*, 10–931. [CrossRef]
13. Cazabat, A.M.; Guena, G. Evaporation of macroscopic sessile droplets. *Soft Matter* **2010**, *6*, 2591–2612. [CrossRef]
14. Girard, F.; Antoni, M.; Faure, S.; Steinchen, A. Influence of heating temperature and relative humidity in the evaporation of pinned droplets. *Colloids Surf. A Physicochem. Eng. Asp.* **2008**, *323*, 36–49. [CrossRef]
15. Velasco-Terán, I.G.; Ancheyta-Palacios, M.; Díaz-Jiménez, L.; Castelán, M.; Carreón, Y.J.; González-Gutiérrez, J. Humidity-regulated drying kinetics and morphological control of protein droplets: Quantitative imaging and classification approaches. *Colloids Surf. A Physicochem. Eng. Asp.* **2025**, *734*, 139393. [CrossRef]
16. Singh, R.; Kaushik, D.; Kamil, S.M.; Satapathy, D.K.; Ghosh, S.K. Ionic liquid-controlled evaporation kinetics of an aqueous sessile drop. *J. Mol. Liq.* **2025**, *418*, 126672. [CrossRef]
17. Gelderblom, H.; Diddens, C.; Marin, A. Evaporation-driven liquid flow in sessile droplets. *Soft Matter* **2022**, *18*, 8535–8553. Correction in *Soft Matter* **2023**, *19*, 2001. [CrossRef] [PubMed]
18. Brutin, D. *Droplet Wetting and Evaporation: From Pure to Complex Fluids*; Academic Press: Cambridge, MA, USA, 2015.
19. Deegan, R.D.; Bakajin, O.; Dupont, T.F.; Huber, G.; Nagel, S.R.; Witten, T.A. Contact line deposits in an evaporating drop. *Phys. Rev. E* **2000**, *62*, 756. [CrossRef] [PubMed]
20. Larson, R.G. Transport and deposition patterns in drying sessile droplets. *AIChE J.* **2014**, *60*, 1538–1571. [CrossRef]
21. Hu, H.; Larson, R.G. Marangoni effect reverses coffee-ring depositions. *J. Phys. Chem. B* **2006**, *110*, 7090–7094. [CrossRef] [PubMed]
22. Still, T.; Yunker, P.J.; Yodh, A.G. Surfactant-induced Marangoni eddies alter the coffee-rings of evaporating colloidal drops. *Langmuir* **2012**, *28*, 4984–4988. [CrossRef] [PubMed]
23. Thayyil Raju, L.; Diddens, C.; Li, Y.; Marin, A.; van der Linden, M.N.; Zhang, X.; Lohse, D. Evaporation of a sessile colloidal water–glycerol droplet: Marangoni ring formation. *Langmuir* **2022**, *38*, 12082–12094. [CrossRef] [PubMed]
24. Le Dizès Castell, R.; Pel, L.; Chekai, T.; Derluyn, H.; Scheel, M.; Jabbari-Farouji, S.; Shahidzadeh, N. Sol-gel transition by evaporation in porous media. *Phys. Rev. Appl.* **2024**, *21*, 034049. [CrossRef]
25. Ikeda, S.; Foegeding, E. Dynamic viscoelastic properties of thermally induced whey protein isolate gels with added lecithin. *Food Hydrocoll.* **1999**, *13*, 245–254. [CrossRef]
26. Pal, A.; Gope, A.; Kafle, R.; Iannacchione, G.S. Phase separation of a nematic liquid crystal in the self-assembly of lysozyme in a drying aqueous solution drop. *MRS Commun.* **2019**, *9*, 150–158. [CrossRef]
27. Clark, A.H. Structural and mechanical properties of biopolymer gels. In *Food Polymers, Gels and Colloids*; Elsevier: Amsterdam, The Netherlands, 1991; pp. 322–338.
28. Van Doorn, J.M.; Bronkhorst, J.; Higler, R.; Van De Laar, T.; Sprakel, J. Linking particle dynamics to local connectivity in colloidal gels. *Phys. Rev. Lett.* **2017**, *118*, 188001. [CrossRef] [PubMed]
29. Tanaka, H. Viscoelastic phase separation. *J. Phys. Condens. Matter* **2000**, *12*, R207. [CrossRef]
30. Carreón, Y.J.; Ríos-Ramírez, M.; Moctezuma, R.; González-Gutiérrez, J. Texture analysis of protein deposits produced by droplet evaporation. *Sci. Rep.* **2018**, *8*, 9580. [CrossRef] [PubMed]
31. Cipelletti, L.; Ramos, L. Slow dynamics in glassy soft matter. *J. Phys. Condens. Matter* **2005**, *17*, R253. [CrossRef]
32. Alshareedah, I.; Borcherds, W.M.; Cohen, S.R.; Singh, A.; Posey, A.E.; Farag, M.; Bremer, A.; Strout, G.W.; Tomares, D.T.; Pappu, R.V.; et al. Sequence-specific interactions determine viscoelasticity and ageing dynamics of protein condensates. *Nat. Phys.* **2024**, *20*, 1482–1491. [CrossRef] [PubMed]
33. Sear, R.P. Non-self-averaging nucleation rate due to quenched disorder. *J. Phys. Condens. Matter* **2011**, *24*, 052205. [CrossRef] [PubMed]
34. Poon, W.C. The physics of a model colloid–polymer mixture. *J. Phys. Condens. Matter* **2002**, *14*, R859. [CrossRef]
35. Bryngelson, J.D.; Onuchic, J.N.; Socci, N.D.; Wolynes, P.G. Funnels, pathways, and the energy landscape of protein folding: A synthesis. *Proteins Struct. Funct. Bioinform.* **1995**, *21*, 167–195. [CrossRef] [PubMed]
36. Sauter, A.; Roosen-Runge, F.; Zhang, F.; Lotze, G.; Feoktystov, A.; Jacobs, R.M.; Schreiber, F. On the question of two-step nucleation in protein crystallization. *Faraday Discuss.* **2015**, *179*, 41–58. [CrossRef] [PubMed]
37. Tanaka, H. Viscoelastic phase separation in soft matter: Numerical-simulation study on its physical mechanism. *Adv. Colloid Interface Sci.* **2006**, *123–126*, 305–325. [CrossRef] [PubMed]

38. Gorr, H.M.; Zueger, J.M.; Barnard, J.A. Lysozyme pattern formation in evaporating drops. *Langmuir* **2012**, *28*, 4039–4042. [CrossRef] [PubMed]
39. Elofsson, C.; Dejmek, P.; Paulsson, M.; Burling, H. Atomic force microscopy studies on whey proteins. *Int. Dairy J.* **1997**, *7*, 813–819. [CrossRef]

**Disclaimer/Publisher's Note:** The statements, opinions and data contained in all publications are solely those of the individual author(s) and contributor(s) and not of MDPI and/or the editor(s). MDPI and/or the editor(s) disclaim responsibility for any injury to people or property resulting from any ideas, methods, instructions or products referred to in the content.